Multiobjective and Multiphysics Design Optimization of a Switched Reluctance Motor for Electric Vehicle Applications

Xiaodong Sun, *Senior Member, IEEE*, Bingkuan Wan, *Student Member, IEEE*, Gang Lei, *Member, IEEE*, Xiang Tian, Youguang Guo, *Senior Member, IEEE*, and Jianguo Zhu, *Senior Member, IEEE*

***Abstract*—Switched reluctance motors (SRMs) have attracted much attention in industry due to the advantages of low cost, robust structure, high fault tolerance and high torque density. However, several disadvantages like high torque ripples and coil temperatures hinder their industrialization for some applications requiring high dynamic performance, like electric vehicles (EVs). In this paper, a multiobjective and multiphysics design optimization method considering both thermal and electromagnetic performance is presented for a 12/10 SRM. First, the topology of the SRM is introduced and the optimal parameters are defined. Then, the electromagnetic finite element model (FEM) is introduced and the 3D transient lumped-parameter thermal model (TLPTM), considering both axial and radial heat transfer for the SRM, is proposed. Second, the objectives and constraints of the optimization are determined. To improve the optimization efficiency, the sequential subspace optimization strategy is employed to find the optimal solution of this high-dimensional design optimization problem. Finally, to validate the effectiveness of the proposed method, both simulation and experimental results are given and discussed. Compared with the initial design, the optimal solution exhibits lower temperature, higher torque, lower torque ripple and less loss.**

***Index Terms*—Multiobjective optimization, multiphysics design, switched reluctance motors (SRMs), thermal analysis.**

I. Introduction

A. Motivation and related research

Nowadays, the development of electric vehicles (EVs) are very rapidly due to environmental pollution and the shortage of oil resources. In recent years, SRMs are becoming popular for industrial applications since they are robust and do not require permanent magnets [1]. However, the temperature rise of the coil and motor housing may be large when operating at high power or for a long time, which hinders their industrialization for some applications requiring high dynamic performance, like EVs [2].

To solve this problem, finite element analysis (FEA) [3] and lumped-parameter thermal model [4] were proposed to figure out the partial or overall temperature of the motor, and the optimization method should be utilized to reduce the temperature. Recently, the FEA and lumped-parameter combined thermal model was proposed to reduce the computational cost using lumped-parameter thermal model in some unimportant parts and improve the accuracy for specific parts using FEA [5]-[6]. The main drawback of this method is the coupling of FEA and lumped-parameter thermal model is particularly complex.

The lumped-parameter thermal model was inspired by common circuits. And the lumped-parameter thermal model mainly includes steady lumped-parameter thermal model (SLPTM) [7] and transient lumped-parameter thermal model (TLPTM) [8]. The main difference between them lies in the existence of thermal capacitance. The Gauss-Seidel method is utilized to solve the temperature node matrix of SLPTM [9]. But the fact is that it may need thousands or tens of thousands of seconds for the temperature of the motor to reach steady-state, which may be hard to monitor the temperature rise for motors.

The temperature of each node for TLPTM can be worked out by circuit simulation and the advantage of TLPTM is that it can reveal the temperature over time. The thermal resistance for teeth and yoke of the stator and rotor can be calculated as hollow cylinder or partial hollow cylinder [8]. But the thermal resistance of the air gap [10], internal air [11]-[12], bearing [12] and housing [13] could only be figured out by experiments. In previous studies [8] and [14], only radial heat transfer was considered for TLPTM.

Various optimization methods for the dimension, shape and topology of the motor were employed in previous studies [15]. And the parameterized geometry [16] and nonparametric geometry [17] are built mainly for dimension and topology optimization, respectively. After determining the type of optimization, four steps should be contained in the typical optimization process: definition of objectives and constraints, definition of the search space, exploration of the solution space, and evaluation and interpretation of the results [18].

Manuscript received Nov. 09, 2020; revised Feb. 09, 2021and Mar. 24; accepted May 02, 2021. This work was supported by the National Natural Science Foundation of China under Project 51875261, the Natural Science Foundation of Jiangsu Province of China under Project BK20180046, and the "Qinglan project" of Jiangsu Province. *(Corresponding author: Gang Lei and Xiang Tian)*

X. Sun, B. Wan, and X. Tian are with the Automotive Engineering Research Institute, Jiangsu University, Zhenjiang 212013, China (email: xdsun@ujs.edu.cn, bingkuan_wan@163.com, auzn0009@163.com).

G. Lei and Y. Guo are with the School of Electrical and Data Engineering, University of Technology Sydney, NSW 2007, Australia (e-mail: Gang.Lei@uts.edu.au, Youguang.Guo-1@uts.edu.au).

J. Zhu is with the School of Electrical and Information Engineering, University of Sydney, NSW, 2006, Australia (e-mail: jianguo.zhu@sydney.edu.au).

In dimension the optimization, the computational burden of FEMs is huge because there are too many design parameters. To solve this problem, the sequential subspace optimization method (SSOM) is utilized. The design parameters are separated and divide them into different subspaces through comprehensive sensitivity analysis. The parameters in different subspaces are featured by their influence for the objectives to prove the mean yield of each parameter in every subspace [19]. Then, subspaces will be optimized in sequence and the termination criterion is defined to find the optimal result [20]-[21]. The interation will be terminated when the termination criterion is satisfied.

Previous research work on the design and optimization method for motors mainly focused on electromagnetic performance, such as torque ripple, torque density or efficiency [22]. The temperature of the motor was utilized to verify the decrease of loss or constraint for a specific component [23]. Although overall temperature can be reduced by decreasing the loss of the motor when optimizing the motor, the geometric shapes, dimensions of the motor and the air flow between stator and rotor will still affect the heat dissipation of the motor. Furthermore, reducing the loss may not reduce the temperature of specific components of the motor.

B. Contribution

This paper investigated the multiobjective optimization of SRMs with the consideration of both thermal and electromagnetic analysis. The main contributions of this paper are listed as follows.

1) A multiphysics optimization method is presented in this study. The SSOM is utilized to reduce the computational burden.
2) The 3D TLPTM is proposed for SRM, which consider both axis and radius direction heat transform. The numeric number of each thermal resistance and capacitance are discussed. The 3D TLPTM can be used as an example not only for SRM but also other types of motor, such as permanent-magnet synchronous motor (PMSM), induction motor (IM) and Synchronous Reluctance Motor (SynRelM).

C. Paper organization

The remainder of this paper is organized as follows. Electromagnetic finite element model (FEM) and 3D TLPTM are introduced in Section II. The layout of the TLPTM for radial and axial direction are displayed. Then, the thermal resistances are calculated and parameterized according to their shape or empirical formula for optimization. Section III presents the multiobjective optimization consisting of comprehensive sensitivity analysis and optimization methods. The SSOM is applied to improve optimization efficiency. Moreover, the optimization results are presented and comprehensive comparisons for the optimal objective between the original and optimal designs are performed. Experiments are performed to verify the optimization results in Section IV, followed by the conclusion.

II. FEM AND 3D TLPTM

A. Parameter calculation and FEM

The 12/10 SRM is utilized as traction machines for EV and scaled-down for a prototype. Fig. 1 shows the topology of the SRM. It is a six-phase motor with 12 stator poles and 10 rotor poles. The last half part of Table I is considered as optimal parameters in that the topology and outside dimension should not be changed during this optimization.

The basic mathematical model of SRM is consist of electromotive force equation and motion equation. The electromotive force equation for phase k can be presented as

$$\begin{cases} U_k = R_k i_k + \dfrac{d\psi_k}{dt} \\ \psi_k = \psi_k(i_k, \theta) \end{cases} \tag{1}$$

where U_k, i_k and R_k is the terminal voltage, phase current and phase resistance of wind for the phase k, respectively. ψ_k and θ is the flux linkage and position of rotor. The motion equation of the motor can be presented as

$$\begin{cases} T_{em} = J\dfrac{d\omega}{dt} + K_\omega \omega + T_L = \dfrac{\partial W'(i_k;\theta)}{\partial \theta} \\ \omega = \dfrac{d\theta}{dt} \end{cases} \tag{2}$$

where T_{em} and T_L is the electromagnetic torque of motor and load torque. J, K_ω and ω is the moment of inertia, frictional coefficient and angular velocity of rotor, respectively. W' is the magnetic coenergy of motor.

TABLE I
INITIAL DESIGN VALUES OF THE SRM

Par.	Description	Unit	Value
n_N	Rated speed	r/min	6000
P_N	Rated power	W	850
m	Number of phases	-	6
N_s	Number of stator poles	-	12
N_r	Number of rotor poles	-	10
$N_{ph}/2$	Turns of each pole	-	25
D_{so}	Stator outer diameter	mm	80
D_{sh}	Shaft diameter	mm	29
l	Axial length	mm	40
D_{ro}	Rotor outer diameter	mm	47
β_s	Stator pole arc	deg.	13.5
β_r	Rotor pole arc	deg.	11.88
h_{cs}	Stator yoke thickness	mm	5
h_{cr}	Rotor yoke thickness	mm	4
g	Air gap	mm	0.5
θ_{on}	Turn-on angle	deg.	-3
θ_{off}	Turn-off angle	deg	10

Several key parameters in Table I, such as the dimensions of stator and rotor laminations, pole arcs and number of turns in each pole will be calculated and discussed as follow [24].

1) Rotor outer diameter and the stack length

The rotor outer diameter D_{ro} and the axial length l of the motor are first estimated by

$$D_{ro}^2 l = k_p \frac{6.1}{B_g A_L} \frac{P_e}{n_N} \tag{3}$$

where k_p is an empirical coefficient related to the phase current. B_g is the airgap flux density at the commutation position. A_L is the electrical load. P_e is the electromagnetic power and the n_N is the rotor speed.

The λ_r is defined as the ratio of l and D_{ro}, and then the reasonable value of B_g, A_L and λ_r are selected. Finally, l and D_{ro} can be calculated after determining the rated power and speed.

2) Air gap

The air gap g has an effect on the inductance at the minimum reluctance position. Considering the assemble technology and safety of the machine, the numeric value of g should not be less than 0.25 mm normally.

3) Pole arc and pole width

The stator and rotor pole arc have an influence on the startup ability at any rotor position for the SRM. According to [25], they are constrained by

$$\begin{cases} \min(\beta_s, \beta_r) \geq \dfrac{2\pi}{mN_r} \\ \beta_s + \beta_r \leq \dfrac{2\pi}{N_r} \end{cases} \tag{4}$$

The stator pole width b_{cs} and rotor pole width b_{cr} can be given by

$$\begin{cases} b_{cs} = (D_{ro} + 2g)\sin(\dfrac{\beta_s}{2}) \\ b_{cr} = D_{ro}\sin(\dfrac{\beta_r}{2}) \end{cases} \tag{5}$$

4) Yoke thickness

Yoke thickness of stator h_{cs} and rotor h_{cr} can be selected by

$$\begin{cases} h_{cs} = (0.7 \sim 1.2)b_{ps} \\ h_{cr} = (0.7 \sim 1.2)b_{pr} \end{cases} \tag{6}$$

5) Number of turns

According to [24], the series turns of each phase N_{ph} can be estimated by

$$N_{ph} = \frac{N_r U_k (\theta_{off} - \theta_{on})}{\omega B_g D_{ro} l \pi} \tag{7}$$

6) Finite element model

The electromagnetic FEM is established in Ansys/Maxwell 2D, as shown in Fig. 1. The control method is angle position control (APC) and the supply voltage is 36 V. The rated speed of the investigated SRM is 6000 r/min.

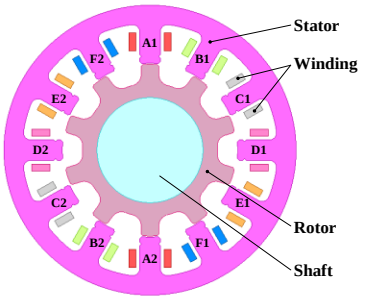

Fig. 1. The 2D Electromagnetic FEM for the SRM.

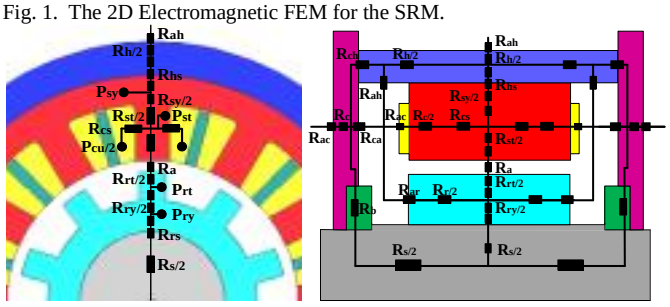

(a) (b)

Fig. 2. Radial and axial heat transfer for the 12/10 SRM. (a) Radial direction, (b) Axial direction.

B. 3D TLPTM

Tradition TLPTM only concerns about the heat transfer for the inner part of the motor in the radial direction [8], as shown in Fig. 2 (a). The heat transfer for axial direction and the outer parts of the motor are shown in Fig. 2 (b). The entire 3D TLPTM is shown in Fig. 3 and mainly includes three components: thermal resistance, controlled heat source, and thermal capacitance. Thermal resistances can be calculated according to their shape and dimension, or empirical formula. The loss of yoke and teeth for the stator and rotor is defined as the controlled heat source and thermal capacitance is utilized to represent the energy storage of stator, rotor, coil and housing.

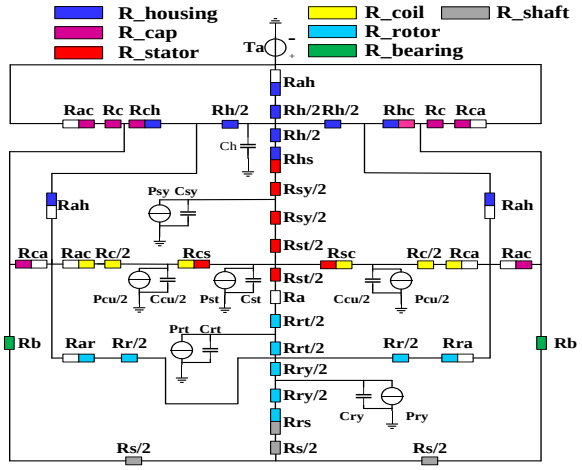

Fig. 3. Entire 3D TLPTM for the 12/10 SRM.

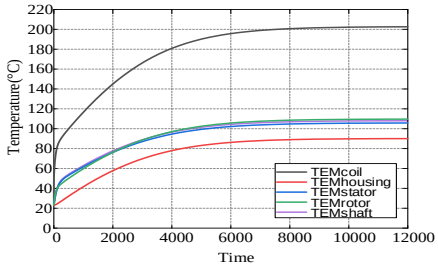

Fig. 4. Transient temperature-time for 3D TLPTM after 12000s.

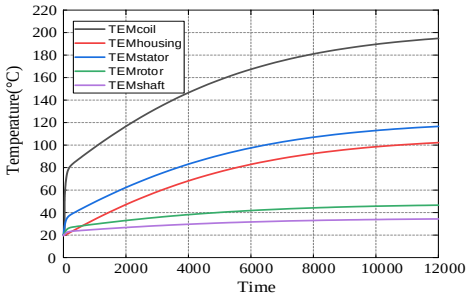

Fig. 5. Transient temperature-time for conventional TLPTM after 12000s.

Thermal analysis should be taken great attention for the 12/10 SRM because the temperature rise will be a serious problem for long time operation. The 3D and conventional TLPTM is built in MATLAB/Simulink and the temperature of the motor after 12000s is shown in Fig. 4 and Fig. 5. The structure of conventional TLPTM is displayed in Fig. 2 (a) [8]. The coil temperatures of 3D and conventional TLPTM are similar because the copper loss is one of the main heat sources

of motor and the thermal capacitance of winding is relatively small. The stator and housing temperatures of 3D TLPTM are smaller than conventional TLPTM because the heat dissipation from the cap to the air is ignored. The rotor and shaft temperatures of conventional TLPTM are much smaller than 3D TLPTM because the axial heat transform of the shaft is ignored.

The temperature classification of the motor winding is A and the maximum temperature rise is 105°C. The initial temperature of the motor is 22°C. Therefore, the temperature of the winding should not be more than 127°C. Considering the temperature margin, the simulation time is set as 600s for this optimization and the temperature of the winding is 103.56°C for 600s after simulation.

1) Thermal resistance for the radial direction

Convection and radiation both exist between air and housing, and natural convection is the main heat transfer mode when the motor is natural cooling [13]. According to [26], the convection coefficient h for round housing can be calculated by a dimensionless equation of Nusselt number Nu, Gasthof Number Gr and Prandtl number Pr

$$h = Nu\lambda_{air} / L \tag{8}$$

$$Nu = a(Gr\,\mathrm{Pr})^b \tag{9}$$

$$Gr = \Delta T \beta G L^3 / \nu_{air}^{\ 2} \tag{10}$$

$$\mathrm{Pr} = c_p \mu / \lambda_{air} \tag{11}$$

where λ_{air} is the conductivity coefficient of air, L is the length of the housing, G is the gravity coefficient and β is the coefficient of volume expansion, which is β=1/(273+T_{air}). T_{air} is the temperature of air. $\triangle T$ is the temperature difference between housing and air. v_{air}, c_p and μ are the kinematic viscosity, specific heat capacity and dynamic viscosity of air, respectively. a and b are the characteristic number concerning the numeric value of $Gr \cdot \mathrm{Pr}$ and the shape of the housing. When the $Gr \cdot \mathrm{Pr}$ is smaller than 10^9, a and b are 0.525 and 0.25 for the round housing, respectively. Otherwise, a and b are 0.129 and 0.33, respectively.

The contact thermal resistance is caused by the air gap between the contact surfaces, which is relevant to material hardness, contact pressure, the roughness of contact surface and atmospheric pressure [9]. The equivalent contact thermal resistance between housing and stator R_{hs} can be calculated as

$$R_{hs} = \frac{\delta_{hs\_equ}}{\lambda_{air} A_{hs\_equ}} \tag{12}$$

where A_{hs_equ} is the contact area of stator and housing, and δ_{hs_equ} is the equivalent air gap between stator and housing. According to [9] and the material of two contact surfaces, the equivalent air gap between the stator and housing δ_{hs_equ}, and rotor and shaft δ_{rs_equ} are defined as 0.045 mm and 0.025 mm, respectively.

The thermal resistance of stator yoke and rotor yoke can be simply obtained directly by the well-known equations of heat transfer in hollow cylinders [27]. The thermal resistance for the outer part of the stator yoke R_{syo} and the inner part of the stator yoke R_{syi} can be calculated as

$$R_{syo} = \frac{1}{2\pi\lambda_{stator} l_s} \ln\left(\frac{r_{syo}}{r_{sym}}\right) \tag{13}$$

$$R_{syi} = \frac{1}{2\pi\lambda_{stator} l_s} \ln\left(\frac{r_{sym}}{r_{syi}}\right) \tag{14}$$

where λ_{stator} and l_s is the conductivity coefficient of silicon steel and the length of the stator, respectively. r_{syo}, and r_{syi} are the outer and inner radius of stator yoke, respectively. And r_{sym} is the average value of stator yoke radius, which is the average value of r_{syo}, and r_{syi}.

The shape of each stator teeth is identical and the overall thermal resistance of the teeth part can be viewed parallel to each tooth [8]. The thermal resistance for the outer part of the stator teeth R_{sto} and the inner part of the stator teeth R_{sti} can be calculated as

$$R_{sto} = \frac{1}{k_{sto} 2\pi\lambda_{stator} l_s} \ln\left(\frac{r_{sto}}{r_{stm}}\right) \tag{15}$$

$$k_{sto} = \frac{S_{teeth\_o}}{\pi(r_{sto}^2 - r_{stm}^2)} \tag{16}$$

$$R_{sti} = \frac{1}{k_{sti} 2\pi\lambda_{stator} l_s} \ln\left(\frac{r_{stm}}{r_{sti}}\right) \tag{17}$$

$$k_{sti} = \frac{S_{teeth\_i}}{\pi(r_{stm}^2 - r_{sti}^2)} \tag{18}$$

where S_{teeth_o} and S_{teeth_i} is the area of the outer and inner part of teeth, respectively. k_{sto} and k_{sti} are the scale factor for the outer and inner part of stator teeth. r_{sto} and r_{sti} are the outer and inner radius of stator teeth, respectively. The r_{stm} is average value of stator yoke radius, which is the average value of r_{sto}, and r_{sti}.

The heat transfer form through the air gap is convection and the Taylor number is utilized to reveal the instability of the air gap [28].

$$\mathrm{Ta} = \frac{\omega^2 \mathrm{r}_g g^3}{\nu_{air}^{\ 2} F_{\mathrm{g}}} = \frac{\omega^2 (0.5 D_{ro} + 0.5g) g^3}{\nu_{air}^{\ 2} F_{\mathrm{g}}} \tag{19}$$

$$Fg = \frac{\pi^4 (D_{ro} + g)}{1967 P D_{ro}} \tag{20}$$

where

$$P = 0.0571(1 - 0.652\frac{g}{0.5D_{ro}}) + 0.00056(1 - 0.652\frac{g}{0.5D_{ro}})^{-1},$$

r_g is the average air gap radius, F_g is the geometric factor.

The critical Taylor number and four modes in the air gap were proved and summarized by Becker and Kaye. But the airflow is driven by continuous and smooth surfaces in previous studies. According to [29], the Nusselt number for the doubly salient structure be can be expressed as

$$\mathrm{Nu} = 0.181 Ta^{0.207} \tag{21}$$

According to the definition of Nusselt number, the thermal resistance of the air gap R_{airgap} can be calculated as

$$h_{airgap} = \frac{Nu\lambda_{air}}{2g} \tag{22}$$

$$R_{airgap} = \frac{1}{h_{airgap} A_{c\_airgap}} = \frac{1}{h_{airgap} 2\pi(0.5D_{ro} + 0.5g)l} \tag{23}$$

where h_{airgap} is the convection coefficient for air flow in air gap and A_{c_airgap} is the cross-section area of the air gap middle surface.

2) Thermal resistance for axial direction

The convection exists between internal air, and inner part of the housing and cap, and overhang of wind and rotor. The experiments were conducted in [11], [12], [30], and empirical formula are given as

$$h_{acap} = h_{ah} = 15 + 6.75(\omega 0.5 D_{ro})^{0.65} \tag{24}$$

$$h_{ca} = 6.5 + 5.25(\omega 0.5 D_{ro})^{0.6} \tag{25}$$

$$h_{ra} = 16.5(\omega 0.5 D_{ro\_y})^{0.65} \tag{26}$$

where h_{acap}, h_{ah}, h_{ca} and h_{ra} are the convection coefficient between internal air and cap, internal air and housing, internal air and end-winding, and internal air and rotor. D_{ro_y} is the rotor yoke outer diameter.

The windings may be distributed in different order and the air gap between insulations are different. It is hard to accurately modeled for each conductor in the slot. To solve this problem, the multilayer winding model [31] and the composite conduction coefficient model [32] were proposed. The composite conduction coefficient model is utilized in this 3D TLPTM and the thermal resistance between wind and stator R_{coil_lam} can be calculated as

$$R_{coil\_lam} = \frac{t_{slot}}{\lambda_{coil\_lam} A_{slot} N_s} \tag{27}$$

$$t_{slot} = \frac{S_{slot}(1 - k_{slot})}{p_{s\_slot}} \tag{28}$$

where t_{slot} is the equivalent thickness for the insulation of the coil. λ_{coil_lam} is the equivalent conductivity coefficient for the insulation of the coil. A_{slot} is the area of stator slot inner surface, S_{slot} is the cross-sectional area of the single slot, k_{slot} is the spacer factor and P_{s_slot} is the circumference of each slot.

Experiments about thermal resistance of bearing were conducted for two motors in [11], and the empirical formula for the thermal resistance of bearing $R_{bearing}$ can be defined as

$$R_{bearing} = 0.45(0.12 - 2r_{bearing\_m})(33 - 2\Omega r_{bearing\_m}) \tag{29}$$

where $r_{bearing\_m}$ is the average radius of bearing and Ω is the mechanical angular frequency of bearing, which is $\Omega = 60 \cdot 2\pi / \omega$. It should be noticed that the formula should be applicable for bearing which is similar to the tested bearing. Requirements are 46 mm$\leq 2r_{bearing} \leq$77.5 mm and $2\omega r_{bearing} \leq$14.5 m/s.

3) Thermal capacitance

Capacitance is an energy storage element in the electric circuit. In 3D TLPTM, thermal capacitance is utilized to represent the energy storage of substances [8]. The thermal capacitance C can be calculated as

$$C = d_s C_s V \tag{30}$$

where d_s, C_s and V are the density, specific heat of the material and the volume, respectively.

III. Multiobjective Optimization Method and Results

A. Optimization model

It is needed to pay more attention to the performance of the output torque, torque ripple, and total loss, which has a great influence on the economy and stability of motor operation. The total loss is the sum of core loss and copper loss. The core loss and current effective value are calculated in the FEMs, and then the copper loss is calculated by the current effective value and phase resistance.

The heat distribution of the motor should also be paid attention to. The stator is the main heat source of housing [33]. Therefore, the stator temperature is defined as the optimal objective to reduce the manufacturing cost of the cooling system. The coil will be tender and easily break off when suffering from high temperature and the copper loss is the main heat source of the internal motor. Therefore, the coil temperatures are defined as optimal objectives and constrain to reduce the inner temperature of the motor and prevent coil breakage caused by excessively high temperatures. The multiobjective model can be defined as

$$\begin{aligned} &\textit{Function}: \min \begin{cases} f_1(TEM_{stator}) \\ f_2(TEM_{coil}) \\ f_3(-T_{out}) \\ f_4(T_{ripple}) \\ f_5(P_{loss}) \end{cases} \\ &\textit{Constraints}: \begin{cases} TEM_{coil} - 107 \leq 0 \\ 1.10 - T_{out} \leq 0 \\ J_c - 5 \leq 0 \end{cases} \end{aligned} \tag{31}$$

where TEM_{stator}, TEM_{coil}, T_{out}, T_{ripple}, P_{loss} and J_c are stator temperature, coil temperature, output torque, torque ripple, total loss, and allowable current density.

To select the optimal solution for a practical application, the selection criterion is defined as

$$\begin{aligned} \min: F = {} & w_1 \frac{TEM_{stator}}{TEM_{stator\_initial}} + w_2 \frac{TEM_{coil}}{TEM_{coil\_initial}} \\ & + w_3 \frac{T_{out\_initial}}{T_{out}} + w_4 \frac{T_{ripple}}{T_{ripple\_initial}} + w_5 \frac{P_{loss}}{P_{loss\_initial}} \end{aligned} \tag{32}$$

where $TEM_{stator\_initial}$, $TEM_{coil\_initial}$, $T_{out\_initial}$, $T_{ripple\_initial}$ and $P_{loss\_initial}$ are the stator temperature, coil temperature, output torque, torque ripple and total loss of the initial design, respectively. w_1, w_2, w_3, w_4 and w_5 are the weighting factors. In this optimization, w_1, w_2, w_3, w_4 and w_5 are assigned as 0.1, 0.1, 0.4, 0.2, and 0.2, respectively.

Kriging model and NSGA II are utilized as the approximate model and optimization algorithms, respectively. The Kriging model is built first, which act as an alternative for FEA and then the NSGA II is utilized to find the Pareto front, based on the data generated by the Kriging model.

The relationship between the objectives and the parameters can be expressed by the Kriging model. Given n sample points

$[\mathbf{x_1}, \mathbf{x_2}, ..., \mathbf{x_n}]$ and their responses $[y(\mathbf{x_1}), y(\mathbf{x_2}), ..., y(\mathbf{x_n})]$, for an input $\mathbf{x}$, the response $y(\mathbf{x})$ of the Kriging model can be expressed as

$$y(\mathbf{x}) = f(\mathbf{x})^T \boldsymbol{\beta} + z(\mathbf{x}) \tag{33}$$

where $f(\mathbf{x})$ is a known approximation model, which is generally assumed as a polynomial and has the form of $f(\mathbf{x})=[f_1(\mathbf{x}), f_2(\mathbf{x}), ..., f_q(\mathbf{x})]^T$, where q is the dimension of polynomial. $\boldsymbol{\beta}$ is the model parameter vector to be estimated. $z(\mathbf{x})$ is usually assumed to be a vector with mean of zero, variance of σ^2, and covariance matrix cov_{ij} as

$$\mathrm{cov}_{ij} = \sigma^2 \mathbf{R}[R(\mathbf{x_i}, \mathbf{x_j})] \tag{34}$$

where $\mathbf{R}$ is the correlation matrix and R is the user-specified correlation function. Gaussian correlation functions are the most commonly utilized model.

B. Comprehensive sensitivity analysis

After the initial design and selection of the desired optimized objectives and constraints, a comprehensive sensitivity analysis method, using Monte Carlo sampling methodology, is utilized to work out the comprehensive sensitivity for the optimal interval. Variance based sensitivity analysis was used in the previous study [34]. The first-order effect index can indicate comprehensive sensitivity and can be expressed as

$$S_i(\mathrm{x}) = \frac{V(E(Y/x_i))}{V(Y)} \tag{35}$$

where $E(.)$ and $V(.)$ represent expectation and variance operators, respectively.

However, it might seem that the computational strategy for the estimation of conditional variance $V(E(f_i(x)/x_j))$ would be cumbersome. To give an indication, if 1000 points were used to get a good estimate of the conditional mean $E(f_i(x)/x_j)$, the procedure will be repeated 1000 times to estimate the variance, then we would need 10^6 points just for one sensitivity index [35]. It is impractical to figure out the first-order effect, even with approximate models.

Sobol' method, which utilizes the quasi Monte-Carlo method, is used to work out the comprehensive sensitivity. First, an $(n,16)$ matrix of Sobol' sequence is generated. Matrix A is the $(n,8)$ preceding matrix column of Sobol sequence and matrix B is the$(n,8)$ rest matrix column of Sobol sequence. Define matrix C_i form by all columns of B except the ith column, which is taken from A. Then, compute the model output for all the input values in the sample matrices A, B, and C_i, obtaining three vectors of model outputs of dimension $n\times 1$:

$$y_A = f(A) \quad y_B = f(B) \quad y_C = f(C) \tag{36}$$

The estimated comprehensive sensitivity indices can be expressed as follow

$$S_i(\mathrm{x}) = \frac{V(E(Y/x_i))}{V(Y)} = \frac{(1/n)\sum_{j=1}^{n} y_A^{(j)} y_{C_i}^{(j)} - f_0^2}{(1/n)\sum_{j=1}^{n} (y_A^{(j)})^2 - f_0^2} \tag{37}$$

where $(.)^{(j)}$ is j column of matrix and

$$f_0^2 = \left(\frac{1}{n} \sum_{j=1}^{n} y_A^{(j)} \right)^2 \tag{38}$$

To solve the problem effectively, a comprehensive sensitivity analysis is adopted to quantitatively investigate the sensitivity of each design variable. The corresponding comprehensive sensitivity function of the motors are defined as

$$\begin{aligned} S(x) = {} & w_1 |S_{TEM_{stator}}(\mathrm{x})| + w_2 |S_{TEM_{coil}}(\mathrm{x})| + w_3 |S_{T_{out}}(\mathrm{x})| \\ & + w_4 |S_{T_{ripple}}(\mathrm{x})| + w_5 |S_{P_{loss}}(\mathrm{x})| \end{aligned} \tag{39}$$

where $|S_{TEMstator}(x)|$, $|S_{TEMcoil}(x)|$, $|S_{Tout}(x)|$, $|S_{Tripple}(x)|$ and $|S_{Ploss}(x)|$ is absolute value of comprehensive sensitivity of stator temperature, coil temperature, output torque, torque ripple and total loss.

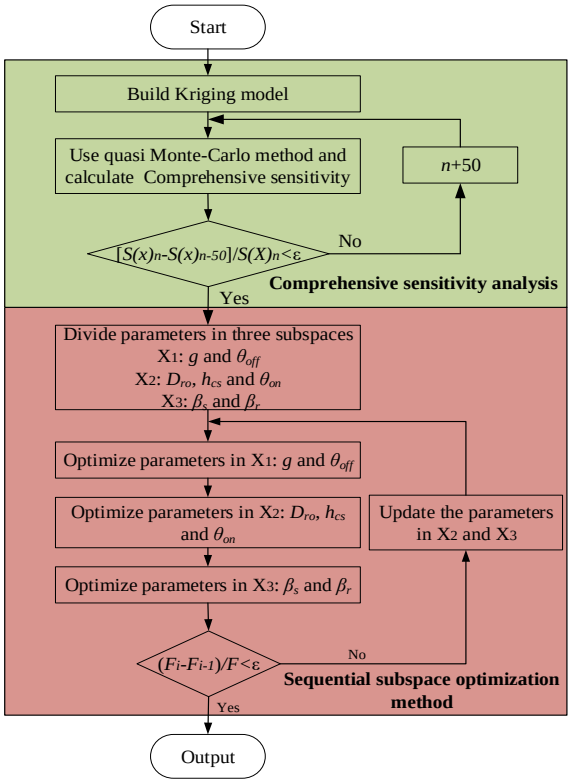

Fig. 6. Flowchart of the multiobjective optimization method for the SRM motor.

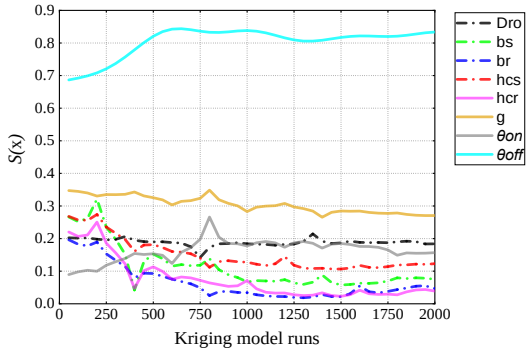

Fig. 7. The convergence of Sobol' method.

Using quasi-random numbers can greatly reduce the total model runs to meet the convergence criteria [35]. However, it still needs hundreds or thousands of FEMs. Therefore, a Kriging model, which can act as an alternative for the FEMs, is built by using 500 FEMs according to Latin hypercube sampling. The strategy for the comprehensive sensitivity analysis is shown in Fig. 6 and the n is the number of Kriging model runs. As shown in Fig. 7, the Sobol' method is conducted every 50 models until meeting convergence criteria, and the

$S(x)$ of each parameter keeps changing before 1000 runs and becomes stable after 1500 runs. The results of comprehensive sensitivity are shown in Table II.

The comprehensive sensitivity ranges from −1 to +1 where a greater magnitude implies a higher sensitivity of an objective with respect to a given variable. A coefficient magnitude above 0.5 is high, resulting in a significant objective value variation for a design. Magnitudes ranging from 0.1 to 0.5 are moderate (representing lower-level effects) and magnitudes below 0.1 are low (almost no change in the objective value). The conclusion that can be drawn from Table II is that each design variable, except rotor yoke thickness h_{cr}, affects at least one objective significantly. Hence, the design variable rotor yoke thickness h_{cr} can be reduced for this application.

TABLE II
COMPRESSIVE SENSITIVITY ANALYSIS VALUE

Var.	Optimization objective					$S(x)$
	$S_{TEMstator}(x)$	$S_{TEMcoil}(x)$	$S_{Tout}(x)$	$S_{Tripple}(x)$	$S_{Ploss}(x)$	
D_{ro}	+0.014	+0.202	+0.337	-0.033	+0.115	0.186
β_s	-0.097	-0.082	-0.095	-0.034	-0.053	0.073
β_r	-0.033	-0.067	-0.072	+0.024	-0.020	0.047
h_{cs}	-0.398	+0.094	+0.091	+0.012	-0.098	0.107
h_{cr}	-0.015	-0.022	-0.037	-0.049	-0.044	0.037
g	+0.437	+0.427	-0.364	+0.024	+0.204	0.277
θ_{on}	-0.133	-0.322	+0.020	-0.368	-0.205	0.168
θ_{off}	+0.741	+0.760	+0.819	-0.772	+0.913	0.814

C. Sequential subspace optimization method

The computation burden can be huge as all optimal interval is taken into consideration because usually only half or whole periodic points need to be calculated [36]. Simultaneously, Kriging model in high dimension is not as accurate as a comparably low dimension, and needs more FEMs and 3D TLPTM. To solve this problem, SSOM is utilized in this optimization. The flowchart of SSOM is shown in Fig. 6 and there are five main steps for each iteration.

Step I Division of the parameters. The parameters are divided into three subspaces X_1, X_2 and X_3, representing highly significant, significant and non-significant subspaces, based on the result of compressive sensitivity analysis in Table II. The air gap g and turn-off angle θ_{off} are divided into subspaces X_1: highly significant; the rotor out diameter D_{ro}, stator yoke thickness h_{cs} and turn-on angle θ_{on} are divided into subspaces X_2: significant; the stator pole arc β_s and rotor pole arc β_r are divided into subspaces X_3: non-significant.

Step II Optimization of the parameters in subspace X_1. The parameters in subspace X_1 are optimized, and the Pareto optimal solution set is worked out when the parameters in subspace X_2 and X_3 are fixed.

Step III Optimization of the parameters in subspace X_2. The parameters in subspace X_2 are optimized, and the Pareto optimal solution set is worked out when the parameters in subspace X_1 and X_3 are fixed, similar to ***Step II***.

Step IV Optimization of the parameters in subspace X_3. The parameters in subspace X_3 are optimized, and the Pareto optimal solution set is worked out when the parameters in subspace X_1 and X_2 are fixed, similar to ***Step II***.

Step V Termination of the optimal solution. ΔF is the difference between two iterations. If their relative error $\Delta F/F$ is smaller than a given value, optimization results/Pareto front will be exported. Otherwise, returning to ***Step II*** with parameters in subspace X_2 and X_3 fixed. The ε is set as 1%.

As illustrated in Fig. 6, the optimization will be terminated when F, defined in (32), meets the convergence criterion. In total, two iteration processes are carried out in this optimization where each iteration contains the sequential optimization of the subspaces of X_1, X_2 and X_3. Figs. 8-9 show the Pareto optimal solutions of each subspace for each iteration and the results of optimal objectives during the optimization. The value of F for Pareto optimal solutions in the first layer will be calculated and select the final optimal solution.

Since $\Delta F/F$ is 0.85% in the second iteration, which is less than 1%, the optimization is terminated after two iterations and output the optimal solution. The optimized parameters of the two iterations are presented in Table III.

TABLE III
OPTIMIZATION RESULTS

Variables	Unit	iteration 1	iteration 2	initial
D_{ro}	mm	48.25	50.24	47.00
β_s	deg	13.98	14.04	13.50
β_r	deg	9	9	11.88
h_{cs}	mm	5.48	5.32	5
g	mm	0.4	0.4	0.5
θ_{on}	deg	-3.04	-2.64	-3
θ_{off}	deg	9.66	9.79	10

The numeric value of F is decreased from 1 to 0.8383, which means the overall performance of the motor improves by 16.17%. The overall comparison between the initial and optimal motor is presented in TABLE IV, and the torque comparison is presented in Fig.10. As shown in Fig.10, the average torque increases by 22.92% and ripple decreases by 34.78%. Fig.11 makes a comparison of the temperature for stator and coil.

TABLE IV
COMPARISON BETWEEN INITIAL AND OPTIMIZED SRM

	TEM_{stator}	TEM_{coil}	T_{out}	T_{ripple}	P_{loss}
Initial	51.53	103.56	0.96	0.31	227.18
Optimal	45.51	88.45	1.18	0.23	207.83
Unit	℃	℃	N • m	-	W

IV. EXPERIMENT AND VALIDATION

A. Verification of FEM for the initial design

Fig. 12 shows the platform for the SSRM drive system, where the 12/10 poles SRM prototype, JN338 torque and speed sensor with 20 Nm torque range, and FZ25J magnetic powder brake with 25 Nm torque range are connected by two couplings. The position is detected by using the Hall sensor ATS675LSE, and then the signal is sent to the dSPACE. Similarly, the current signal captured by the current sensor is sent to the dSPACE for further control. The sampling time is set as 1 ms. Other hardware includes a DC power supply, an asymmetrical half-bridge circuit, a PC and an oscilloscope.

The measured torque and current are shown in Fig. 13 and Fig. 14. The experimental output torque is 0.98 and torque ripple is 0.34, which conforms to the simulation results. The

comparison between simulated and measured temperature for stator and coil are presented in Fig. 15. As shown in Fig. 4, the temperature of the coil, rotor, stator and housing reached 202° C, 113°C, 106°C and 90 °C when reaching steady-state, which must be not applicable in the laboratory. Considering the winding temperature for the initial design and temperature margin as mentioned above, the temperatures of the motor are measured for every 30s and the duration of the experiment is 600s, which is parallel to the simulation time of the optimization.

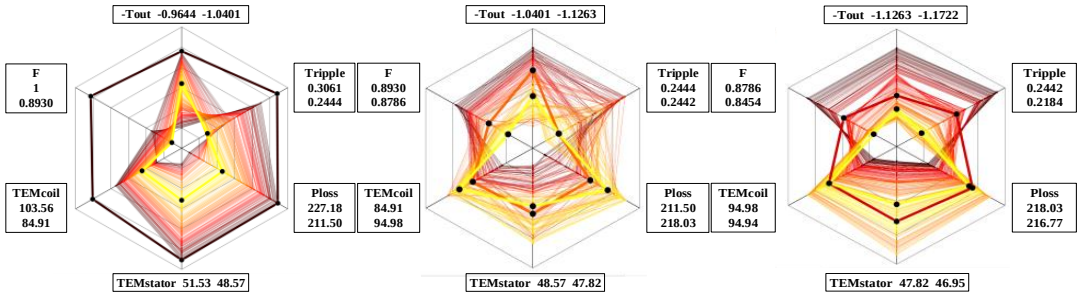

(a) (b) (c)

Fig. 8. Pareto optimal solutions of iteration 1. (a) Subspace X_1, (b) Subspace X_2, (c) Subspace X_3.

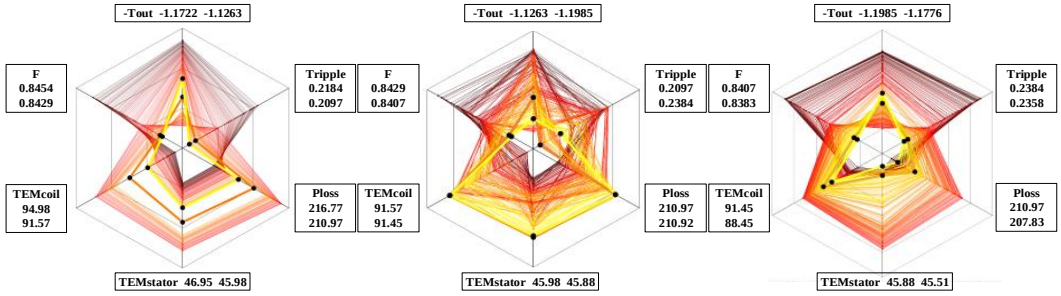

(a) (b) (c)

Fig. 9. Pareto optimal solutions of iteration 2. (a) Subspace X_1, (b) Subspace X_2, (c) Subspace X_3.

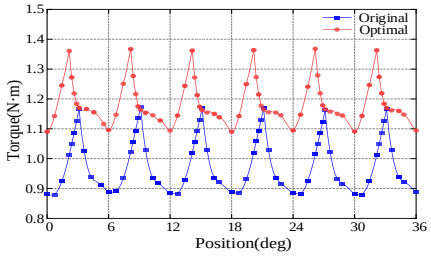

Fig. 10. Comparison of torque between the original and optimal solutions.

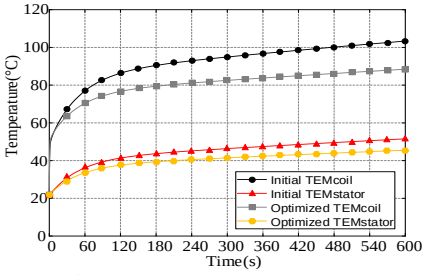

Fig. 11. Comparison of temperatures between the initial and optimal solutions.

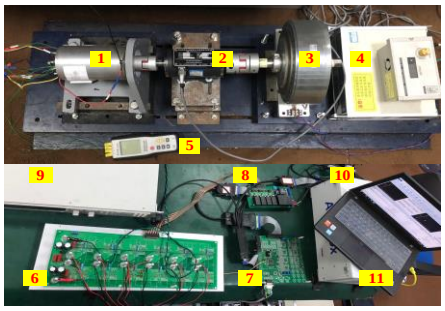

Fig. 12. Platform of the investigated SRM motor. (1) The 12/10 SRM. (2) Torque and speed sensor. (3) Magnetic power brake. (4) Torque and rotational speed measurer. (5) Thermocouple (6) Power converter. (7) Conditioning board. (8) Driving circuit. (9) Power supply. (10) dSPACE. (11) PC.

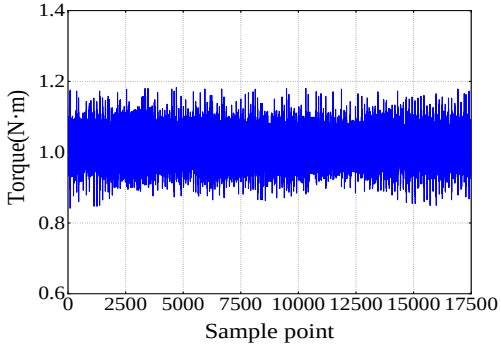

Fig. 13. Experimental output torque result under APC at speed 6000 r/min.

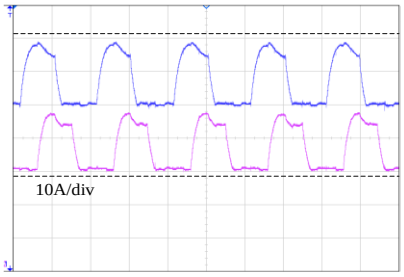

Fig. 14. Experimental current for phase A and B under APC at speed 6000 r/min.

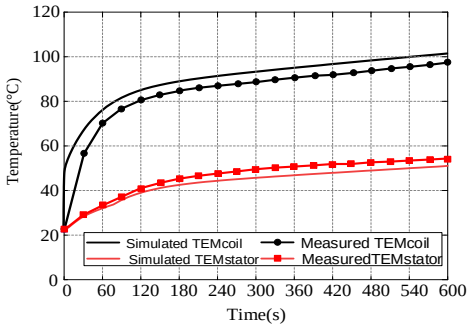

Fig. 15. Measured and simulated temperatures for coil and stator.

V. Conclusion

A multiphysics field collaborative optimization method based on SSOM was presented to improve the thermal and electromagnetic performance for a 12/10 SRM.

After analyzing the radial and axial heat transfer of the motor, the 3D TLPTM, considering both axial and radial heat transfer for the SRM, was constructed. The thermal resistances were gathered and summarized. The 3D TLPTM can reduce the computation burden and improve the accuracy of the lumped-parameter thermal model.

The NSGA II was utilized to find the best performance of those optimal objectives in terms of temperature, torque, torque ripple and total loss. A comprehensive sensitivity analysis was conducted based on the Sobol' method. Then, parameters were divided into three subspaces and optimized in sequence. Finally, an optimal solution has been selected according to the defined selection criterion after two iteration processes. The results show that comprehensive sensitivity analysis can reveal the uncertain affected by the parameters during the whole optimal interval. The approximate model can act as an alternative for FEMs and 3D TLPTM and reduce the computation burden of the sensitivity analysis. The multiphysics field collaborative optimization method can improve the performance of the SRM in both thermal and electromagnetic fields. The stator temperature, coil temperature, torque ripple and total loss were reduced by 11.68%, 14.59%, 25.80% and 8.51%, respectively. And the torque improved by 22.91%.

References

[1] X. Sun, K. Diao, G. Lei, Y. Guo, and J. Zhu, "Direct torque control based on a fast modeling method for a segmented-rotor switched reluctance motor in HEV application," *IEEE J. Emerg. Sel. Topics Power Electron.*, vol. 9, no. 1, pp. 232-241, Feb. 2021.

[2] X. Sun, Z. Shi, G. Lei, Y. Guo, and J. Zhu, "Analysis and Design Optimization of a Permanent Magnet Synchronous Motor for a Campus Patrol Electric Vehicle," *IEEE Trans. Veh. Technol.*, vol. 68, no. 11, pp. 10535-10544, Nov. 2019.

[3] N. Arbab, W. Wang, C. Lin, J. Hearron, and B. Fahimi, "Thermal Modeling and Analysis of a Double-Stator Switched Reluctance Motor," *IEEE Trans. Energy Convers.*, vol. 30, no. 3, pp. 1209-1217, Sep. 2015.

[4] B. Su, X. Sun, L. Chen, Z. Yang, and K. Li, "Thermal modeling and analysis of bearingless permanent magnet synchronous motors," *Int. J. Appl. Electrom. Mech.*, vol. 56, no. 1, pp. 115-130, Jan. 2018.

[5] S. Nategh, O. Wallmark, M. Leksell, and S. Zhao, "Thermal Analysis of a PMaSRM Using Partial FEA and Lumped Parameter Modeling," *IEEE Trans. Energy Convers.*, vol. 27, no. 2, pp. 477-488, 2012.

[6] K. Diao, X. Sun, G. Lei, Y. Guo, and J. Zhu, "Multiobjective system level optimization method for switched reluctance motor drive systems using finite element model," *IEEE Trans. Ind. Electron.*, vol. 67, no. 12, pp. 10055-10064, Dec. 2020.

[7] S. Li, S. Zhang, T. G. Habetler, and R. G. Harley, "Modeling, Design Optimization, and Applications of Switched Reluctance Machines—A Review," *IEEE Trans. Ind. Appl.*, vol. 55, no. 3, pp. 2660-2681, 2019.

[8] S. Song, W. Liu, and U. Schaefer, "Thermal Analysis of a 30kW Switched Reluctance Starter/Generator System Used in Aircraft," in *Proc. IEEE POWERENG*, Lisbon, 2009, pp. 331-336.

[9] F. Cheng and J. Lin, *Modern motor design*. China: China Machine Press, 1993.

[10] D. A. Howey, P. R. N. Childs, and A. S. Holmes, "Air-Gap Convection in Rotating Electrical Machines," *IEEE Trans. Ind. Electron.*, vol. 59, no. 3, pp. 1367-1375, Mar. 2012.

[11] G. Kylander, *Thermal modelling of small cage induction motors*. Chalmers University of Technology, 1995.

[12] J. J. L. t. Lindström, Chalmers University of Technology, Göteborg, Sweden, "Thermal model of a permanent-magnet motor for a hybrid electric vehicle," 1999.

[13] A. Boglietti, A. Cavagnino, and D. A. Staton, "TEFC induction motors thermal models: a parameter sensitivity analysis," *IEEE Trans. Ind. Appl.*, vol. 41, no. 3, pp. 756-763, Jun. 2005.

[14] W. Wang, J. Zhao, Y. Zhou and F. Dong, "New optimization design method for a double secondary linear motor based on R-DNN modeling method and MCS optimization algorithm," *Chinese Journal of Electrical Engineering*, vol. 6, no. 3, pp. 98-105, Sept. 2020.

[15] Z. Ling, J. Ji, T. Zeng and W. Zhao, "Design optimization and comparison of linear magnetic actuators under different topologies," *Chinese Journal of Electrical Engineering*, vol. 6, no. 1, pp. 41-51, March 2020.

[16] C. Ma and L. Qu, "Multiobjective Optimization of Switched Reluctance Motors Based on Design of Experiments and Particle Swarm Optimization," *IEEE Trans. Energy Convers.*, vol. 30, no. 3, pp. 1144-1153, Sep. 2015.

[17] S. Sato, T. Sato, and H. Igarashi, "Topology Optimization of Synchronous Reluctance Motor Using Normalized Gaussian Network," *IEEE Trans. Magn.*, vol. 51, no. 3, pp. 1-4, Mar. 2015.

[18] G. Bramerdorfer, J. A. Tapia, J. J. Pyrhönen, and A. Cavagnino, "Modern Electrical Machine Design Optimization: Techniques, Trends, and Best Practices," *IEEE Trans. Ind. Electron.*, vol. 65, no. 10, pp. 7672-7684, Oct. 2018.

[19] C. J. Wu and M. S. Hamada, *Experiments: planning, analysis, and optimization*. John Wiley & Sons, 2011.

[20] X. Sun, Z. Shi, and J. Zhu, "Multi-objective design optimization of an IPMSM for EVs based on fuzzy method and sequential Taguchi method," *IEEE Trans. Ind. Electron.*, 2021, DOI: 10.1109/TIE.2020.3031534, to be published.

[21] H. Li and C. Chang, "Recursive Orthogonal Projection-Based Simplex Growing Algorithm," *IEEE Trans. Geosci Remote Sens*, vol. 54, no. 7, pp. 3780-3793, Jul. 2016.

[22] X. Sun, Z. Shi, Y. Cai, G. Lei, Y. Guo, and J. Zhu, "Driving-cycle oriented design optimization of a permanent magnet hub motor drive system for a four-wheel-drive electric vehicle," *IEEE Trans. Transport. Electrific.*, vol. 6, no. 3, pp. 1115-1125, Sep. 2020.

[23] X. Sun, Y. Shen, S. Wang, G. Lei, Z. Yang, and S. Han, "Core losses analysis of a novel 16/10 segmented rotor switched reluctance BSG motor for HEVs using nonlinear lumped parameter equivalent circuit model," *IEEE/ASME Trans. Mechatronics*, vol. 23, no. 2, pp. 747-757, Apr. 2018.

[24] X. Sun, L. Feng, K. Diao, and Z. Yang, "An improved direct instantaneous torque control based on adaptive terminal sliding mode for a segmented-rotor SRM," *IEEE Trans. Ind. Electron.*, 2021, DOI: 10.1109/TIE.2020.3029463, to be published.

[25] R. Krishnan, *Switched Reluctance Motor Drives: Modeling, Simulation, Analysis, Design, and Applications*. CRC Press, 2001.

[26] D. A. Staton and A. Cavagnino, "Convection Heat Transfer and Flow Calculations Suitable for Electric Machines Thermal Models," *IEEE Trans. Ind. Electron.*, vol. 55, no. 10, pp. 3509-3516, Oct. 2008.
[27] P. S. Ghoshdastidar, *Heat Transfer*. India: Oxford University Press, 2004.
[28] Ketchum and B. Carl, "An Experimental Study of Baroclinic Annulus Waves at Large Taylor Number," *J. Atmos. Sci.*, vol. 29, no. 4, pp. 665-679, Sep. 2010.
[29] P. Romanazzi and D. A. Howey, "Air-gap Convection in a Switched Reluctance Machine," in *Proc. IEEE EVER*, Monte Carlo, 2015, pp. 1-7.
[30] G. D. Demetriades, H. Z. De La Parra, E. Andersson, and H. Olsson, "A real-time thermal model of a permanent-magnet synchronous motor," *IEEE Trans. Power Electron.*, vol. 25, no. 2, pp. 463-474, Jul. 2009.
[31] A. Boglietti, A. Cavagnino, and D. Staton, "Determination of Critical Parameters in Electrical Machine Thermal Models," *IEEE Trans. Ind. Appl.*, vol. 44, no. 4, pp. 1150-1159, Jul. 2008.
[32] D. Staton, A. Boglietti, and A. Cavagnino, "Solving the more difficult aspects of electric motor thermal analysis in small and medium size industrial induction motors," *IEEE Trans. Energy Convers.*, vol. 20, no. 3, pp. 620-628, Sep. 2005.
[33] S. Ulbrich, J. Kopte, and J. Proske, "Cooling Fin Optimization on a TEFC Electrical Machine Housing Using a 2-D Conjugate Heat Transfer Model," *IEEE Trans. Ind. Electron.*, vol. 65, no. 2, pp. 1711-1718, Feb. 2018.
[34] Z. Shi, X. Sun, Y. Cai, and Z. Yang, "Robust design optimization of a five-phase PM hub motor for fault-tolerant operation based on Taguchi method," *IEEE Trans. Energy Convers.*, vol. 35, no. 4, pp. 2036-2044. Dec. 2020.
[35] A. Saltelli, M. Ratto, T. Andres, F. Campolongo, J. Cariboni, D. Gatelli, M. Saisana, and S. Tarantola, *Global sensitivity analysis: the primer*. John Wiley & Sons, 2008.
[36] X. Sun, Z. Shi, G. Lei, Y. Guo, and J. Zhu, "Multi-objective design optimization of an IPMSM based on multilevel strategy," *IEEE Trans. Ind. Electron.*, vol. 68, no. 1, pp. 139-148, Jan. 2021.

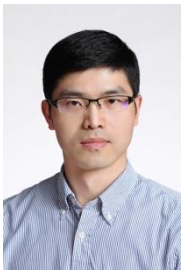

Xiaodong Sun (M'12-SM'18) received the B.Sc. degree in electrical engineering, and the M.Sc. and Ph.D. degrees in control engineering from Jiangsu University, Zhenjiang, China, in 2004, 2008, and 2011, respectively.

Since 2004, he has been with Jiangsu University, where he is currently a Professor in Vehicle Engineering with the Automotive Engineering Research Institute. From 2014 to 2015, he was a Visiting Professor with the School of Electrical, Mechanical, and Mechatronic Systems, University of Technology Sydney, Sydney, Australia. His current teaching and research interests include electrified vehicles, electrical machines, electrical drives, and energy management. He is the author or coauthor of more than 100 refereed technical papers and one book, and he is the holder of 42 patents in his areas of interest. Dr. Sun is an Editor of the IEEE TRANSACTIONS ON ENERGY CONVERSION.

Bingkuan Wan (S'21) was born in Nanjing, Jiangsu, China, in 1997. He received the B.S. degree in vehicle engineering from Tianjin University of Science and Technology, Tianjin, China, in 2019, and he is currently working toward the M.E. degree in Jiangsu University, Zhenjiang, China.

His current research interests include design and optimization of electrical drive systems.

Gang Lei (M'14) received the B.S. degree in Mathematics from Huanggang Normal University, China, in 2003, the M.S. degree in Mathematics and Ph.D. degree in Electrical Engineering from Huazhong University of Science and Technology, China, in 2006 and 2009, respectively.

He is currently a Senior Lecturer at the School of Electrical and Data Engineering, University of Technology Sydney (UTS), Australia. His research interests include computational electromagnetics, design optimization and control of electrical drive systems and renewable energy systems. He is an Associate Editor of the IEEE TRANSACTIONS ON INDUSTRIAL ELECTRONICS and an Editor of the IEEE TRANSACTIONS ON ENERGY CONVERSION.

Xiang Tian was born in Zhenjiang, Jiangsu, China, in 1983. He received the B.S. degree in electrical engineering, M.S. degree in power electronics and power transmission and Ph.D. degree in vehicle engineering from Jiangsu University, Zhenjiang, China, in 2006, 2009 and 2018, respectively. He is currently a lecturer with the automotive engineering research institute, Jiangsu University.

His current research interests include electric vehicles, hybrid electric vehicles, parameter matching, optimal energy control strategy, and vehicle powertrain control.

Youguang Guo (S'02-M'05-SM'06) received the B.E. degree from Huazhong University of Science and Technology, China in 1985, the M.E. degree from Zhejiang University, China in 1988, and the Ph.D. degree from University of Technology Sydney (UTS), Australia in 2004, all in electrical engineering.

He is currently a Professor at the School of Electrical and Data Engineering, UTS. His research fields include measurement and modeling of properties of magnetic materials, numerical analysis of electromagnetic field, electrical machine design optimization, power electronic drives and control.

Jianguo Zhu (S'93–M'96–SM'03) received the B.E. degree in 1982 from Jiangsu Institute of Technology, Jiangsu, China, the M.E. degree in 1987 from Shanghai University of Technology, Shanghai, China, and the Ph.D. degree in 1995 from the University of Technology Sydney (UTS), Sydney, Australia, all in electrical engineering.

He was appointed a lecturer at UTS in 1994 and promoted to full professor in 2004 and Distinguished Professor of Electrical Engineering in 2017. At UTS, he has held various leadership positions, including the Head of School for School of Electrical, Mechanical and Mechatronic Systems and Director of Centre for Electrical Machines and Power Electronics. In 2018, he joined the University of Sydney, Australia, as a full professor and Head of School for School of Electrical and Information Engineering. His research interests include computational electromagnetics, measurement and modelling of magnetic properties of materials, electrical machines and drives, power electronics, renewable energy systems and smart micro grids.